Nonlinear Characterization for Microstrip Circuits With Low Passive Intermodulation

Alexey P. Shitvov, *Member, IEEE*, Dmitry S. Kozlov, and Alexander G. Schuchinsky, *Fellow, IEEE*

***Abstract*— Products of passive intermodulation (PIM) generated by weak nonlinearities of passive circuits subjected to relatively high transmit power of multicarrier signals may cause strong interference in emerging broadband and multiradio communication systems. This paper presents a new approach to a characterization of distributed nonlinearities in printed circuits fabricated on commercial grade microwave laminate materials. An efficient procedure for PIM characterization has been devised using the commercial RF-CAD software. The phenomenological model has been developed to take into account concurrent distributed nonlinearities of printed transmission lines and to evaluate PIM products of arbitrary order. It has been observed for the first time that the sources of nonlinearity in typical microstrip circuits may have highly uneven distributions which require a different means for PIM characterization and modeling. The proposed methodology has been validated by accurate predictions of the PIM response of complex circuit layouts. The results of this paper pave the way to a holistic approach to the design of planar microwave circuits and devices under given linearity constraints.**

***Index Terms*— Circuit characterization, distortion measurement, intermodulation distortion, nonlinear distortion, printed circuits.**

I. Introduction

PLANAR microwave technologies are a cornerstone of RF front-end and base-station antennas for emerging wireless communications. Modern RF laminate materials enable high-performance distributed circuits and multilayer integration that suit a wide range of communications frequencies. While the state-of-the-art materials feature low loss and dispersion, excellent thermal and mechanical properties, as well as tight fabrication tolerances at relatively low cost, the actual device performance often conspicuously deviates from the predictions. This is particularly related to the linearity of passive microwave circuits, such as planar filters, phase shifters, and multiplexers, exposed to relatively high-power multicarrier analog and digital signals in frequency division duplex base-station antennas and other passive devices, [1].

Intrinsic weak nonlinearities of the materials and contacts in printed circuits are manifested in generation of intermodulation products, known as passive intermodulation (PIM). It is a known cause of signal distortion in terrestrial wireless [1], satellite [2], and marine [3] communications. A number of studies have been undertaken in the past decades to elucidate PIM causes and to identify mechanisms of nonlinearity in passive microwave components, [4], [5]. However, PIM characterization and mitigation by design still remain elusive and highly empirical tasks. This is partly due to the limitations of the existing test instruments, [6]. Advanced PIM measurement systems and methodologies, including the multicarrier [2], vector [7], broadband [8], and range detection [9] systems, often have insufficient resolution and sensitivity. Besides, the experimental data are rarely insightful due to the lack of proven theoretical models of PIM generation. The temperamental and multiphysics nature of the PIM phenomena also hamper the development of realistic computational models of the effects of distributed nonlinearity in complex microwave devices and systems. In spite of that, a number of real-time adaptive algorithms and hardware solutions have recently been proposed for PIM cancelation in base-station antennas, [10]. They are directly derived from the amplifier and transmitter linearization methodologies with little effort made to account for the distinctive features of PIM generation. As a result, the proposed solutions often fail to achieve the sought PIM mitigation efficiency in practice.

Basic signal impairments in printed circuits caused by the intrinsic electrical nonlinearities of strip conductors and substrate materials along with the electro-thermal effects have been studied. In particular, superconducting microstrip lines (SCML) were analyzed in [11]–[13], and tunable microstrip lines on ferroelectric [14], [15] and liquid crystal substrates [16] were investigated. The reported numerical and experimental studies of the third-order intermodulation (IM3) in SCML resonators and filters, [13], [17]–[19], revealed some characteristic features which suggested a means of suppressing the nonlinear response by optimizing the filter topology. In particular, it was suggested that the PIM generation due to the intrinsic superconductor nonlinearity can be reduced by increasing the width of the transmission line (TL) sections, thus decreasing the current density on the strip. Also, optimum combination of individual resonator Q-factors, resonance frequencies, and their locations was sought with the aid of the simulated annealing technique, [13]. It was observed that directly reducing the peak current density in the selected

Manuscript received June 20, 2017; revised September 8, 2017; accepted September 22, 2017. This work was partially funded by FP7 Marie Curie ITN ARTISAN under Grant 316426. This paper is an expanded version from the International Workshop on Integrated Nonlinear Microwave and Millimeter-Wave Circuits, Graz, Austria, April 20–21, 2017. *(Corresponding author: Alexey P. Shitvov.)*

A. P. Shitvov is with the School of Electronics, Electrical Engineering and Computer Science, Institute of Electronics, Communications and Information Technology, Queen's University Belfast, Belfast BT3 9DT, U.K. (e-mail: alexey795@google.com).

D. S. Kozlov is with Nokia Bell-Labs, D15Y6NT Dublin, Ireland (e-mail: dmitry.1.kozlov@nokia.com).

A. G. Schuchinsky is with the Department of Electrical Engineering and Electronics, University of Liverpool, Liverpool L69 3GJ, U.K. (e-mail: a.schuchinsky@liverpool.ac.uk).

Color versions of one or more of the figures in this paper are available online at http://ieeexplore.ieee.org.

Digital Object Identifier 10.1109/TMTT.2017.2758726

resonators that contribute stronger to the total IM response does not necessarily result in the minimum IM level at the device ports, [13], which indicated the need of a holistic approach to the resonator and filter design with low PIM.

A distinct aspect of the published works is the use of specific physical models of intrinsic nonlinearity. While being phenomenological and subject to experimental validation, such models were based on the predefined physical mechanisms, e.g., an assumed dependence of the superfluid density on the electric current density in superconductors, [20], or electrothermal coupling in imperfect conductors, [21], [22]. In contrast, characterization of the intrinsic nonlinearities in planar circuits fabricated on commercial RF laminates and operated in a broad temperature range is complicated by that the dominant mechanisms and location of nonlinearities are typically unknown *a priori*. So, the net nonlinear response is rendered by multiple concurrent sources that may vary in time under influence of various factors. The great diversity and variability of the TL nonlinearities, including both distributed and lumped (e.g., contact) sources, along with limited capabilities of the scalar PIM measurements, require a different approach to characterization, modeling, and mitigation of PIM in planar microwave circuits and devices.

To address the aforementioned problems, a "black-box" approach has been adopted for the design of complex distributed circuits under the linearity constraints. The network behavioral models based on the memoryless polynomial transfer functions, [23], and the models with memristors, [24], have been proposed for PIM simulations. However, such models retrieved from the measurement data usually lack a physical insight in the causes and physical mechanisms of nonlinearity.

In this paper, we present an efficient approach to accurate characterization of the PIM sources and mechanisms of intrinsic nonlinearities in microstrip lines when the parameters of nonlinearity are retrieved from two-tone scalar PIM measurements. In contrast to the earlier works, [25], [26], the presented approach allows us to simulate the effects of multiple nonlinear sources and account for the high-order effects under the assumption of weak nonlinearity. A simple, physics-based analytical model of distributed PIM generation in uniform microstrip lines is presented in Section II. Its implementation and the use in the commercial RF CAD software with harmonic balance solver are discussed in Section III. The model capability of the PIM characterization and prediction is demonstrated by the example of a low-pass stepped-impedance microstrip filter in Section IV. The main results and implications for the design of low-PIM microstrip filters and circuits are summarized in the conclusion.

II. Theoretical Model of Distributed PIM

Building on the previous works, [25], [26], the PIM analysis is based on a generalized model of TL with weak distributed nonlinearity (TLDN). Both conductor and substrate nonlinearities are described by the local static polynomials, which are inherently similar to the high-order sinusoidal input describing functions.

The use of the memoryless polynomial model, on the one hand, is consistent with the measurement data acquired with the commercial PIM analyzers and, on the other hand, is justified by our experimental observations. Indeed, a typical two-tone PIM analyzer permits measurement only of a lower-sideband PIM product magnitude with minimum 200 kHz (few megahertz in case of the third-order PIM) offset of the CW carrier frequencies. This proved to be insufficient for detection of the low-frequency dynamics, such as electrothermal, [21], [22], and memory effects, whereas the instruments capable of the extended nonlinear characterization have the residual PIM level higher than that in the low-PIM PCB laminates. While the dynamic nonlinearity of passive devices may affect practical signal waveforms, the available data suggest that its effect is hardly discernible, as compared with the static nonlinearity. Indeed, the frequency-sweep measurements of PIM products of different orders on the test microstrip lines used in our study have demonstrated constant PIM level across the whole Rx-band when either of two carrier frequencies swept across the Tx-band. The PIM level also remains frequency invariant when the carrier power varies. Therefore, in this paper, we adopt the static polynomial model that can be deduced from the data acquired with the aid of commercial PIM analyzers. Then the distributed PIM process can be described by the circuit model of TLDN, Fig. 1, with the nonlinear per-unit-length (p.u.l.) parameters represented in the polynomial form, as follows, see [27], [28]:

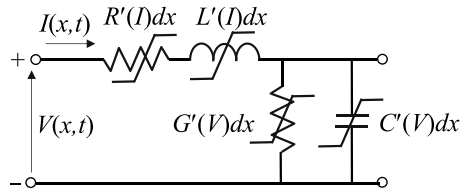

Fig. 1. Circuit model for incremental length of a nonlinear TL.

$$
\begin{aligned}
R'(I) &= \sum_{n=0}^{(N-1)/2} R'_{2n} I^{2n} = R'_0 + R'_{NL}(I) \\
L'(I) &= \sum_{n=0}^{(N-1)/2} L'_{2n} I^{2n} = L'_0 + L'_{NL}(I) \\
C'(V) &= \sum_{n=0}^{(N-1)/2} C'_{2n} V^{2n} = C'_0 + C'_{NL}(V) \\
G'(V) &= \sum_{n=0}^{(N-1)/2} G'_{2n} V^{2n} = G'_0 + G'_{NL}(V) \qquad (1)
\end{aligned}
$$

where N is an odd integer, $I(x,t)$ and $V(x,t)$ are the complex-valued current and voltage waveforms, and R'_{2n}, L'_{2n}, C'_{2n}, and G'_{2n} are the linear parameters of the TL at $n = 0$ and at $n > 0$ they represent the TL nonlinearity with the phenomenological parameters retrieved from the experimental data.

It is noteworthy that while the polynomial model (1) formally describes generation of harmonics and mixing products of multicarrier signals, the phenomenological parameters of TLDN are physically meaningful and can be associated with the dominant mechanism of nonlinearity. Validity of approximations (1) for the nonlinear parameters of the TLDN, as the power series of I^2 and V^2, has been verified by cross-band PIM measurements of the test microstrip lines. The second-

order PIM (PIM2) products generated by two carriers with frequencies from the E-GSM 900 Tx-band and their second harmonics were measured in the PCS 1900 Rx-band. The measured level of the PIM2 products at the carrier power of 44 dBm was below the instrument noise floor of −90 dBm, whereas the measured third-order PIM (PIM3) products were above −80 dBm. These results have demonstrated the dominant contribution of the odd-order PIM products and thus justified the nonlinearity model (1).

The effect of the microstrip line geometry on the TLDN parameters can be approximately taken into account with the aid of the geometrical factor, [13]. Using the model of parallel-plate waveguide with uniform distributions of current density, fields in the substrate and sources of nonlinearity across the signal strip, the linear and nonlinear parameters of the model (1) are determined from a quasi-static analysis as

$$R'_{2n} = \frac{\rho_{2n}}{\delta_s^{2n+1} w^{2n+1}} \qquad L'_{2n} = \frac{\mu_{2n} h^{2n+1}}{w^{2n+1}}$$
$$C'_{2n} = \frac{\varepsilon'_{2n} w_{eff}}{h^{2n+1}} \qquad G'_{2n} = \frac{\omega\, \varepsilon''_{2n} w_{eff}}{h^{2n+1}} \tag{2}$$

where w and h are the microstrip linewidth and substrate height, respectively, w_{eff} is the effective width of the signal strip, [29], ω—angular frequency, and δ_s—skin depth. The phenomenological parameters ρ_{2n}, μ_{2n} and $\varepsilon_{2n} = \varepsilon'_{2n} - j\varepsilon''_{2n}$ describe the conductor resistivity $\rho(J) = \sum_{n=0}^{(N-1)/2} \rho_{2n} J^{2n}$, permeability $\mu(H) = \sum_{n=0}^{(N-1)/2} \mu_{2n} H^{2n}$, and complex permittivity of the substrate $\varepsilon(E) = \sum_{n=0}^{(N-1)/2} \varepsilon_{2n} E^{2n}$, where J, E, and H are the magnitudes of the complex vectors of the electric current density on the signal strip and of the electric and magnetic fields in the substrate. The linear p.u.l. parameters R'_0, L'_0, C'_0, and G'_0 can be calculated in the quasi-static approximation and related directly to the microstrip geometry and linear constitutive parameters, whereas the coefficients of the nonlinear terms are deduced here from the measurement data. In some cases, if the mechanisms of nonlinearity are known, the coefficients of the nonlinearity can also be derived from the underlying physical model, see [20].

Considering the phenomenological model (1), the nonlinear voltage and current waveforms on a uniform TLDN can be described by the generalized telegrapher's equations, see [25], [27], [28]

$$\frac{\partial I(x,t)}{\partial x} = -C'_0 \frac{\partial V(x,t)}{\partial t} - G'_0 V(x,t) - \frac{\partial I_{NL}(x,t)}{\partial x}$$
$$\frac{\partial V(x,t)}{\partial x} = -L'_0 \frac{\partial I(x,t)}{\partial t} - R'_0 I(x,t) - \frac{\partial V_{NL}(x,t)}{\partial x}. \tag{3}$$

In fact, (3) describes a TL with a voltage-controlled current source and a current-controlled voltage source, given by

$$\frac{\partial I_{NL}(x,t)}{\partial x} = \frac{\partial (C'_{NL}(V) V(x,t))}{\partial t} + G'_{NL}(V) V(x,t)$$
$$\frac{\partial V_{NL}(x,t)}{\partial x} = \frac{\partial (L'_{NL}(I) I(x,t))}{\partial t} + R'_{NL}(I) I(x,t). \tag{4}$$

Taking the derivative of the first equation in (3) with respect to x and the second equation with respect to t, after straightforward algebraic manipulations we can obtain the inhomogeneous wave equation for the current waveform $I(x,t)$

$$\frac{\partial^2 I(x,t)}{\partial x^2} = L'_0 C_0 \frac{\partial^2 I(x,t)}{\partial t^2} + (R'_0 C'_0 + G'_0 L'_0) \frac{\partial I(x,t)}{\partial t} + G'_0 R'_0 I(x,t) + C'_0 \frac{\partial^2 V_{NL}(x,t)}{\partial x \partial t} + G'_0 \frac{\partial V_{NL}(x,t)}{\partial x} - \frac{\partial^2 I_{NL}(x,t)}{\partial x^2}. \tag{5}$$

In the case when the source signal contains two carriers with frequencies ω_1 and ω_2, the TL nonlinearity causes generation of harmonics of the carrier frequencies and intermodulation products. Therefore, the steady-state propagating, $I(x,t)$, and regenerating, $I_{NL}(x,t)$, current waveforms can be represented in time domain by double Fourier series [4], that is,

$$I(x,t) = \sum_{m=-\infty}^{\infty} \sum_{n=-\infty}^{\infty} \hat{I}_{mn}(x) e^{j\omega_{mn} t}$$
$$I_{NL}(x,t) = \sum_{m=-\infty}^{\infty} \sum_{n=-\infty}^{\infty} \hat{I}_{NL_{mn}}(x) e^{j\omega_{mn} t} \tag{6}$$

and similarly for $V(x,t)$ and $V_{NL}(x,t)$. In (6), the spectral frequencies are defined as $\omega_{mn} = m\omega_1 + n\omega_2$. Substituting (6) into (4), and similarly for the voltage waveforms, and collecting the terms at each frequency ω_{mn}, the corresponding nonlinear voltage and current sources can be expressed as

$$\frac{d\hat{I}_{NL_{mn}}(x)}{dx} = \sum_{l=1}^{(N-1)/2} (j\omega_{mn} C'_{2l} + G'_{2l}) F_{mn}\{V^{2l+1}(x,t)\}$$
$$\frac{d\hat{V}_{NL_{mn}}(x)}{dx} = \sum_{l=1}^{(N-1)/2} (j\omega_{mn} L'_{2l} + R'_{2l}) F_{mn}\{I^{2l+1}(x,t)\} \tag{7}$$

where the operator $F_{mn}\{\cdots\}$ gives the spatially variable complex Fourier amplitude of its argument at frequency ω_{mn}. It accounts for all contributions by low- and high-order terms in (6) mixed via (4) down to frequency ω_{mn}. Then substituting (6) into (5) gives the equations for complex amplitudes of the spectral components at each frequency ω_{mn}

$$\frac{d^2 \hat{I}_{mn}(x)}{dx^2} - \gamma_{mn}^2 \hat{I}_{mn}(x) = \frac{\gamma_{mn}}{Z_{c_{mn}}} \frac{d\hat{V}_{NL_{mn}}(x)}{dx} - \frac{d^2 \hat{I}_{NL_{mn}}(x)}{dx^2} \tag{8}$$

where γ_{mn} and $Z_{c_{mn}}$ are the propagation constant and characteristic impedance at frequency ω_{mn}, respectively,

$$\gamma_{mn} = \sqrt{(R'_0 + j\omega_{mn} L'_0)(G'_0 + j\omega_{mn} C'_0)} \approx \alpha_{mn} + j\beta_{mn}$$
$$Z_{c_{mn}} = \sqrt{(R'_0 + j\omega_{mn} L'_0)/(G'_0 + j\omega_{mn} C'_0)}.$$

In general, the set of equations in (8) for all spectral components $\hat{I}_{mn}(x)$ of the propagating current waveform $I(x,t)$ in (6) represents a system of coupled linear equations. The coupling is due to the source terms in the right-hand side of (8). The latter terms are obtained from (7) by substituting the Fourier-series expansions of the propagating current and voltage waveforms, $I(x,t)$ and $V(x,t)$, and calculating the corresponding operators. System (8) can be solved by successive iterations taking into account the contributions from

the mixing low-order terms, see [25], [27], [28]. In this paper, we limit the analysis to the simpler case, where the voltage and current waveforms in the right-hand side of (7) are represented by the two-tone carrier waveforms only, thus neglecting the contributions from the low-order mixing products and thus effectively decoupling the equations in (8). This approximation proved to be a fairly accurate for a weak nonlinearity. Besides, the inaccuracy inflicted by series truncation can be recompensed through the phenomenological parameters in (1).

Under the assumptions made, the resulting decoupled equations are solved at each intermodulation frequency of interest, $\omega_M = [(M+1)\omega_1 - (M-1)\omega_2]/2$, for the respective PIM current distribution (note that hereafter we use index M to replace the double index mn, where $m = M+1$ and $n = M-1$, and M is an odd integer and positive for the lower sideband PIM products if $\omega_1 < \omega_2$). The power of the forward and reverse PIM products of Mth order at the output and input of a matched uniform TL with $|\beta_1 - \beta_2|L \ll 1$ reads

$$P_{fwd_M}(L) = \frac{1}{2} Re\{Z_{c_M}\} |A_M|^2 (|M|-1)^2 \alpha^2 L^2 e^{-2\alpha L}$$
$$P_{rev_M}(L) = \frac{1}{2} Re\{Z_{c_M}\} \frac{|A_M|^2}{\beta_M^2} (|M|-1)^2 \alpha^2 \sin^2(\beta_M L) \quad (9)$$

where v_p is the phase velocity of the carriers in the TL

$$A_M = \sum_{l=1}^{(N-1)/2} \left[\binom{2l+1}{l+1} \frac{\hat{I}_0}{Z_0} |\hat{I}_0|^{2l} \binom{2l+1}{l+1-(M+1)/2} \times \frac{X_M}{2^{2l}(\chi_M^2 - \gamma_M^2)} \right]$$
$$X_M = \gamma_M (j\omega_M L'_{2l} + R'_{2l}) + \chi_M Z_{c_M}^2 |Z_{c_M}|^{2l} (j\omega_M C'_{2l} + G'_{2l})$$
$$\gamma_M = \sqrt{(R'_0 + j\omega_M L'_0)(G'_0 + j\omega_M C'_0)}$$
$$Z_{c_M} = \sqrt{(R'_0 + j\omega_M L'_0)/(G'_0 + j\omega_M C'_0)}$$
$$\chi_M = |M|\alpha + j[(M+1)\beta_1 - (M-1)\beta_2]/2$$

and $\binom{k}{l}$ are the binomial coefficients, $\hat{I}_0$ is the complex current amplitude at a carrier frequency (we assume equal amplitudes of in-phase carriers), and α is the attenuation constant assumed to be the same at the carrier frequencies and intermodulation frequencies, i.e., $\alpha_M = \alpha$.

The closed-form expressions (9) for the power of the forward and reverse PIM products of arbitrary order M on a matched TLDN and small dispersion have been obtained for the generic static polynomial model (1) of Nth order. Consistently with, [25], (9) shows that the power of the forward PIM products grows monotonically with the TL length at $\alpha L \ll 1$, and power of the reverse PIM products has regular undulation as the TL length increases and do not vanish even on the matched TL.

Although (9) has been derived in the parallel-plate strip approximation, the effects of transversely nonuniform current and field distributions in microstrip TL can be taken into account in (9) by correcting the geometrical factors in (2), see [13]. Equations (9) can, in principle, be used directly to characterize the TL nonlinearity defined by (1). The number of significant phenomenological parameters can be also reduced, e.g., by adopting a different model of nonlinearity, as demonstrated further in this paper. In Section IV, it will be shown that the nonanalytical polynomial of the type $R'(I) = \sum_{n=0}^{N} R'_n |I|^n$ provides more compact approximation of the TLDN nonlinear resistance. Note that the modulus polynomial can be easily incorporated in (9) by modifying the binomial coefficients and powers in A_M, see [27].

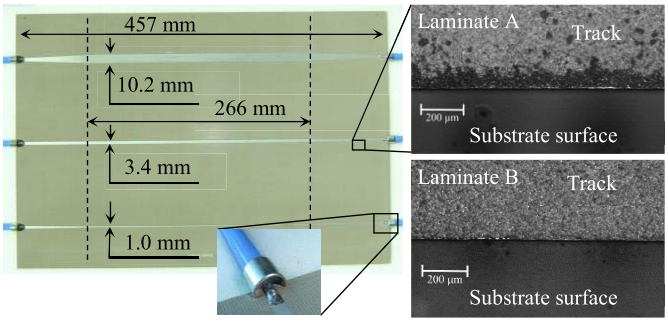

Fig. 2. PCB with microstrip TLs of different widths (the reference uniform TL has the track width of 3.4 mm) and an enlarged view of the track edge showing "black-tin" contamination, alongside the high-quality plating, [26].

III. Model Validation

To verify the outlined model, microstrip TLs of different width shown in Fig. 2 have been simulated and measured, [26]. Two identical specimens containing two tapered and one uniform microstrip TLs of different width were fabricated. The reference uniform 50-Ω TL has the track width of 3.4 mm. The lengths of the narrow and wide TLs were matched to the 50 Ω input and output terminals by seven-section Klopfeinstein tapers. Each set of three lines was fabricated on a single PCB panel, identified as Laminates A and B, respectively.

The two PCB materials are commercial PTFE/ceramic-based laminates (dielectric constant = 3.5, dissipation factor = 0.002, and substrate thickness $h = 1.52$ mm) with a low profile 1 oz. copper cladding. Laminate A is a high-performance material qualified for low-PIM base-station antenna applications, whereas Laminate B is a low-cost RF material. The conductor patterns are finished with a 1 μm immersion-tin plating processed by the same PCB workshop. Despite different substrates, the conductor material and patterns on the two panels were identical. However, visual inspection revealed that the strip edges on Laminate A panel were contaminated by the "black-tin,"[1] whilst quality of plating on Laminate B panel was good, as shown in Fig. 2.

The microstrip lines were fit with low-PIM microstrip launchers made of high-performance coaxial cable assemblies. Fig. 3 shows the results of the PIM measurements using a Rosenberger rack-type PIM analyzer unit, [31]. The instrument allows concurrent measurements of multiple PIM products at the input (reverse PIM) and output (forward PIM) of the device under test with the residual PIM level below −125 dBm for two 43 dBm carriers. The reverse PIM products were measured at the microstrip input when the output was terminated in a low-PIM broadband load. The lower sideband PIM3 products

[1]The "black-tin" contamination is a persistent issue in tin plating, often attributed to deposition of cupric ions on tin, iron contamination or other processes caused by excessive acidity in plating bath, [30].

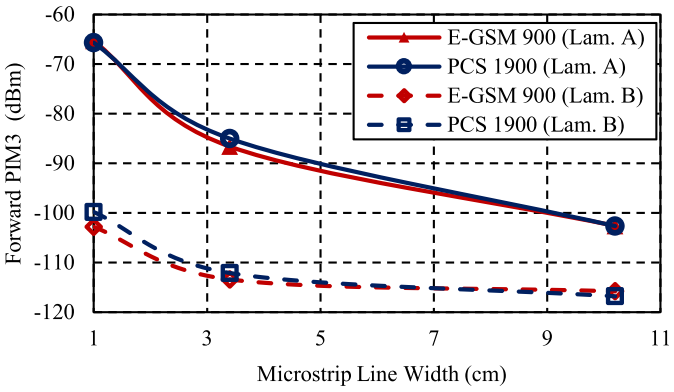

Fig. 3. Forward PIM3 products measured on the test microstrip TLs of different widths in E-GSM 900 and PCS 1900 bands at 40 dBm carrier power.

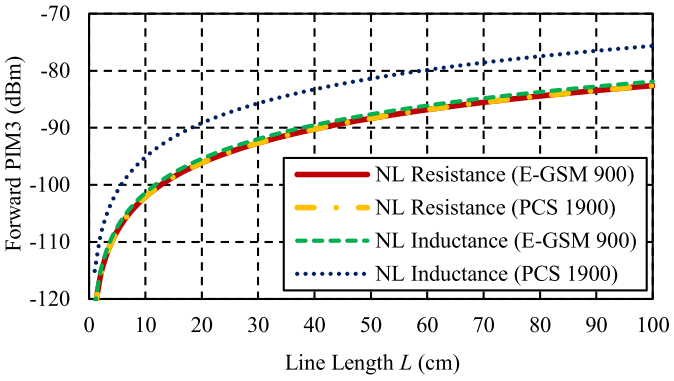

Fig. 4. Simulated forward PIM3 products versus the TL length, assuming either dominant nonlinear p.u.l. resistance or inductance, when the carrier frequencies are in either E-GSM 900 or PCS 1900 bands.

were measured at E-GSM 900 frequency $f_{IM3} = 2f_1 - f_2 = 910$ MHz, with the carrier frequencies $f_1 = 935$ MHz and $f_2 = 960$ MHz, and at PCS 1900 frequency $f_{IM3} = 1870$ MHz, with the carrier frequencies $f_1 = 1930$ MHz and $f_2 = 1990$ MHz. The measured PIM level in the samples on Laminate A appears to be more than 30 dB higher than that on Laminate B.

The higher PIM on Laminate A is attributed to the additional nonlinearity of the strip edges tainted by "black-tin." Indeed, the measurement results in Fig. 3 show that the PIM3 level decreases with the strip width and barely differs in the two frequency bands. Such trends are inherent to the dominant conductor nonlinearity, as PIM on wider strip decreases due to lower current density of high-power carriers and the effect of the return current on the ground plane is much weaker, [32].

To further verify the dominant contribution of the resistive nonlinearity, PIM products were simulated in the TL with either p.u.l. nonlinear resistance or p.u.l. nonlinear inductance described by the polynomial approximations (1) with $N = 3$. The coefficients R_2' and L_2' were determined by fitting the simulated two-tone forward PIM3 products (9) to the measured ones on the reference Laminate A uniform microstrip TL at frequency of 910 MHz and two 40 dBm CW carriers. The simulation results in Fig. 4 show that in the case of the inductive nonlinearity the level of forward PIM3 should be noticeably higher in PCS 1900 band than in E-GSM 900.

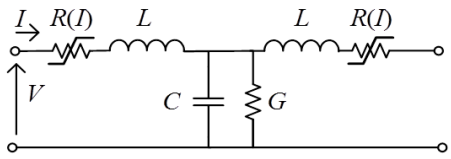

Fig. 5. RF-CAD model of a TL unit cell of electrical length $\theta_0 = 15°$ at frequency 910 MHz, [26].

Conversely, it remains practically unchanged in the case of resistive nonlinearity. This confirms the negligible effect of inductive nonlinearity deduced from the PIM3 measurements on Laminate A in Fig. 3. Alternatively, the resistive and inductive nonlinearities can be discriminated using the simultaneous measurements of the third-order PIM and third-harmonic products, see [28].

The presented model of distributed PIM generation has been developed for matched TLDNs. It can be extended to account for arbitrary nonlinear terminations and lumped nonlinearities, albeit the closed-form expressions become more involved. Furthermore, analytical modeling of practical printed circuits with complex layouts becomes virtually intractable. Therefore, an alternative approach based on the harmonic balance analysis implemented in commercial RF-CAD software has been adopted for PIM analysis and used in the rest of this paper. Nevertheless, the developed analytical models remain invaluable tools providing insight in the mechanisms of distributed PIM generation and effects of the TL geometry. They also enable extraction of the geometry-independent phenomenological parameters of nonlinearities and provide a benchmark for the numerical analysis.

IV. RF-CAD Model of TLDN

The harmonic balance solver in Keysight Advanced Design Studio (ADS) software, [33], has been adopted for simulating the PIM in printed circuits. To illustrate its utility, PIM products in microstrip TLs with the current-driven nonlinear resistivity have been simulated and compared with the measurement results of Section III. A circuit model of the uniform TLDN was devised by partitioning the line length into identical short sections. Each unit cell was described by an equivalent T-network, Fig. 5, and its small-signal circuit parameters were obtained by the conventional quasi-static analysis. The electrical length of each segment was chosen to be 15° at 910 MHz, which provided the input return loss better than 20 dB across a broad frequency range, up to the third harmonic of the carrier. The reference cells were cascaded to form 45° intermediate sections and then simulated. For a longer TL, each intermediate section was described by the X-parameters used for subsequent nonlinear cascading. This approach allows simulation of the forward and reverse PIM products of arbitrary order, as well as PIM product distribution along the TL with the 15° resolution. Unless otherwise stated, all the results below are presented for the E-GSM 900 band and PIM3 frequency $f_{PIM3} = 910$ MHz.

The nonlinear resistances in the equivalent circuit of the 15° long T-cell in Fig. 5 were extracted by fitting to the forward PIM3 products measured on the reference uniform microstrip TL on Laminate A when the carrier power varied

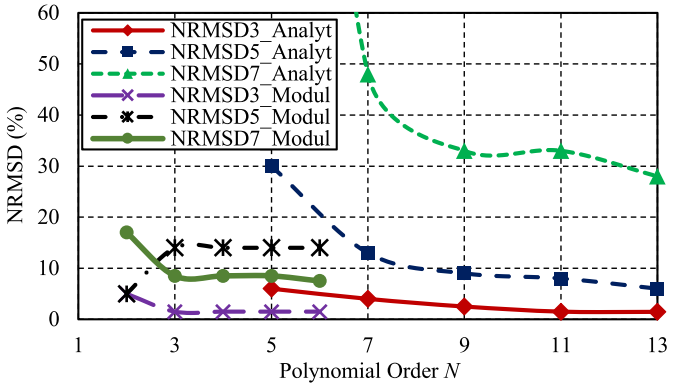

Fig. 6. NRMSDs PIM product fitting versus the polynomial degree for the PIM products of different order using analytical and modulus polynomial models.

TABLE I

EXTRACTED RESISTIVE NONLINEARITY PARAMETERS (15° UNIT CELL, FIG. 5) FOR THE REFERENCE UNIFORM MICROSTRIP LINE ON LAMINATE A PANEL

n	R_n (Ohm/A^n)	
	Analytical Polynomial $R(I)=R_0+\sum_{n=1}^{(N-1)/2} R_{2n}I^{2n}$	Modulus Polynomial [26] $R(I)=R_0+\sum_{n=1}^{N} R_n\lvert I\rvert^n$
0	0.01178	0.01178
1	2.81659×10^{-6}	1.27621×10^{-6}
2	-9.61792×10^{-7}	6.039×10^{-7}
3	1.77514×10^{-7}	0
4	-9.98443×10^{-9}	0

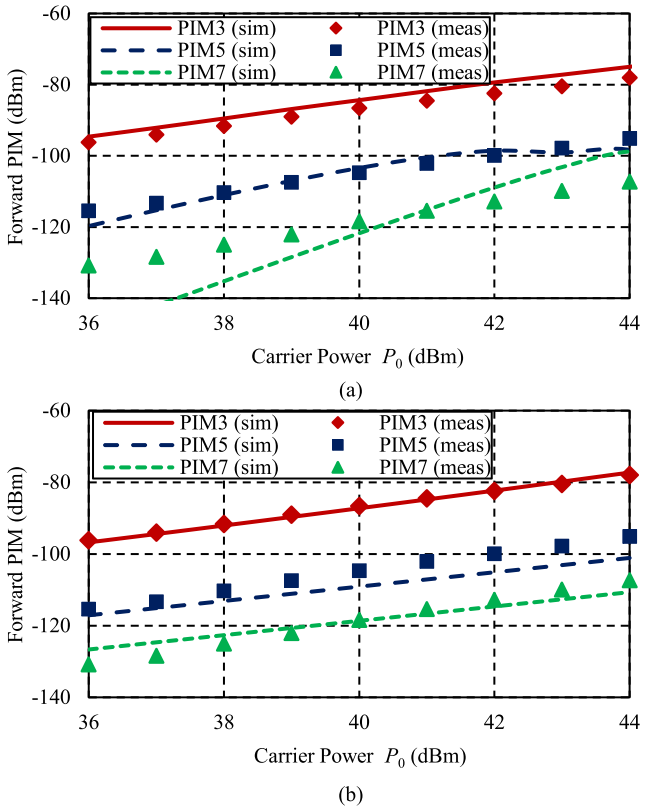

Fig. 7. High-order forward PIM products versus carrier power P_0 measured and simulated, using (a) analytical and (b) modulus polynomial models in Table I, see [26].

from 30 to 44 dBm. Taking advantage of the ADS HB capability of working with user defined nonlinear models, two different polynomial approximations have been employed, viz., the analytical polynomial, $R(I) = R_0 + \sum_{n=1}^{(N-1)/2} R_{2n} I^{2n}$, and the modulus polynomial, $R(I) = R_0 + \sum_{n=1}^{N} R_n |I|^n$, [26]. It is worth noting that neither of the two models produces even-order IM and harmonic terms. The unknown nonlinearity parameters were retrieved with the standard optimization toolbox in the Keysight ADS by minimizing the goal function using the gradient optimization algorithm, where the goal function was defined by the root-mean-square deviation between the simulated and measured forward PIM3 products (in dBm) in a range of carrier power from 36 to 44 dBm. The normalized root-mean-square deviation (NRMSD) of the PIM product fitting shown in Fig. 6 decreases as the polynomial order increases and approaches a constant residual error of ~1.5%. For the analytical polynomial, the minimum error is achieved when its order is at least $N = 9$, whereas $N = 3$ suffices for the modulus polynomial. The residual error in both cases can be attributed to the PIM measurement uncertainties. The respective polynomial coefficients are summarized in Table I.

Given that the polynomial coefficients were extracted by fitting to the measured forward PIM3 products on the uniform microstrip line in the specified power range, accuracy of the retrieved models had to be verified by simulation of the reverse PIM3 and high-order PIM products, as well as their dependence on the microstrip TL width. In Fig. 7, the measured data for the fifth-order (PIM5) and seventh-order (PIM7) IM products on the reference uniform TL are juxtaposed with the respective simulation results based upon the coefficients extracted from the forward PIM3 measurements (see Table I). A peculiar feature of the experimental data is that the slopes of the forward PIM products of different orders versus the carrier power are nearly identical. The NRMSD convergence for both polynomial models of different PIM products is shown in Fig. 6. The simulations suggest that accuracy of the analytical polynomial approximation can be improved with the use of higher order polynomials, so that the analytical polynomial reaches the NRMSD similar to that of the modulus polynomial of order $N = 3$ for all PIM products, see [34]. These observations suggest that the modulus type polynomial model better represents the experimental data and thus suits well the CAD assisted analysis of distributed PIM generation in planar microwave circuits.

The effect of the microstrip TL width was examined with the aid of the analytical polynomial model specified in Table I. Fig. 8 shows the simulation and measured results for the forward PIM3 products at different carrier power levels. The simulated dependence on the microstrip TL width was obtained by scaling the small-signal TL parameters and nonlinear resistance coefficients of Table I in accordance with (2). Good agreement of the simulations with the experiment, suggests that the adopted parallel-plate model of microstrip line is adequate for the analysis. The small discrepancies for the microstrip TL of width $w = 10.2$ mm are due to the

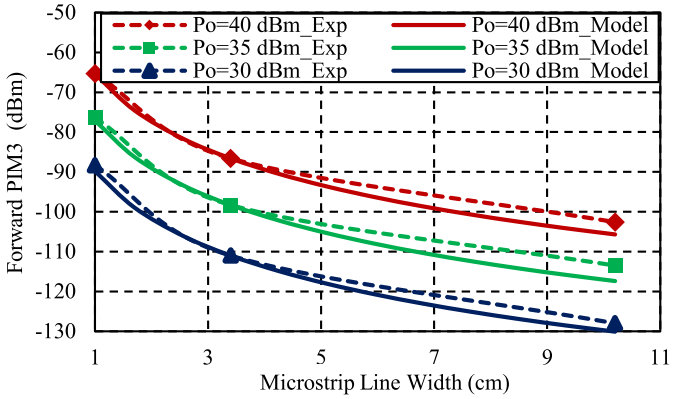

Fig. 8. Simulated and measured forward PIM3 products versus the microstrip width at different carrier power levels, see [26].

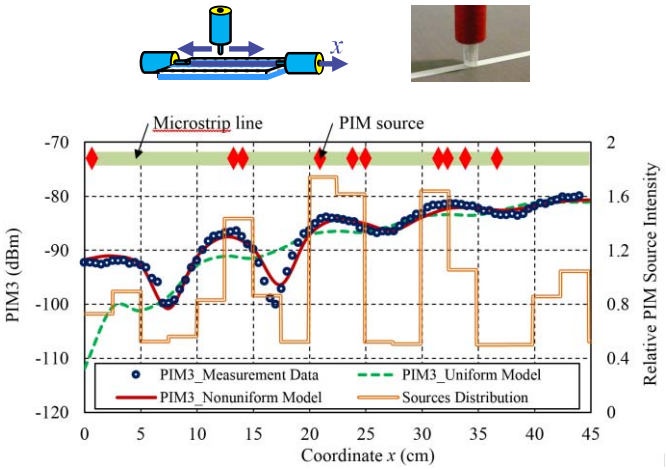

Fig. 9. Near-filed mapping and simulations of the PIM3 distribution along the reference uniform microstrip line on Laminate A panel. The "PIM nonuniform model" plot was simulated using the relative PIM source intensity (right axis), [26]. Also depicted are the positions of large "black-tin" clusters (red diamonds) along the TL (green strip) revealed by visual inspection.

effect of the tapers and feed sections, see Fig. 1, which had not been deembedded in Fig. 8 and were perceived to have a greater effect for the wide microstrip line where the wide section contributes less to the net PIM response.

Given the superior performance of the modulus-polynomial model, it has been adopted for the harmonic balance CAD analysis of a simple low-pass stepped-impedance filter discussed in Section VI.

V. Near-Field PIM Mapping

To gain a deeper insight in the process of distributed PIM generation, the PIM3 products have been mapped by near-field probing along the reference uniform microstrip line at frequency $f_{IM3} = 910$ MHz and carrier power of 43 dBm. A low-PIM open-ended coaxial E-field probe was connected to the receiver port of the PIM analyzer, while the TL under test was terminated in a broadband low-PIM load. Fig. 9 shows the calibrated results of the near-field mapping in comparison with the two simulated curves. One simulation ("uniform model") was performed by concatenating identical 15°-long unit cells with the parameters of nonlinear resistance specified in Table I. The other curve ("nonuniform model")

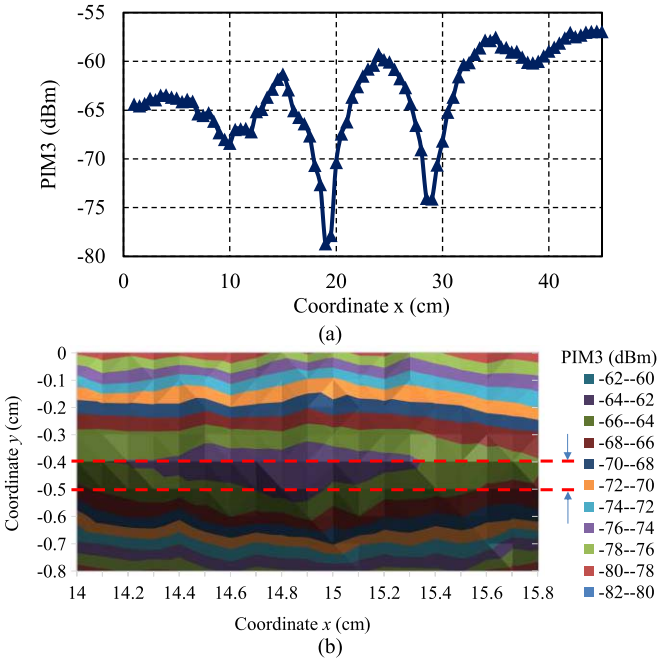

Fig. 10. (a) Near-field mapping of the PIM3 magnitude distribution along the center of the narrow microstrip line ($w = 1$ mm, indicated by dashed red lines) and (b) about a PIM3 peak at $x = 14.9$ cm in (a). The measurements in (b) were made at $f_{IM3} = 910$ MHz and carrier power 43 dBm with a 1 mm increment.

was obtained by cascading three consecutive 15° unit cells into 45° sections and scaling the nonlinear coefficients of each 45° section in accordance with the nonuniform source distribution ("sources distribution"). The weighted PIM source intensity is used as the scaling factor for the constituent 15° unit cells relative to those of the "uniform model." The PIM intensity distribution was estimated by fitting to the measured curve and it appeared to be fairly well correlated with the actual distribution of the larger clusters of "black-tin" specks on the signal strip observed in visual inspection. The results in Fig. 9 suggest that nonuniform distribution of microscopic nonlinear sources is likely to be responsible for the discrepancy between the simulated and measured reverse PIM3 level at the input of the uniform TL.

The distribution of PIM3 intensity along the narrow microstrip TL ($w = 1$ mm shown in Fig. 2) on Laminate A obtained by near-field probing is shown in Fig. 10(a). A zoomed pattern of the PIM3 distribution near a peculiar peak at distance $x = 14.9$ cm from the TL input is plotted in Fig. 10(b). It shows noticeably higher PIM level at one edge of the track, although no considerable "black-tin" contamination was detected by visual inspection.

These observations reveal two important features of the distributed PIM generation that require certain flexibility of the RF-CAD model presented in Section IV: 1) several PIM sources may act concurrently or dominate in certain frequency/power range and 2) the TL nonlinearities may be very irregularly distributed along and across the strip conductor, and can appear as a few relatively strong localized sources.

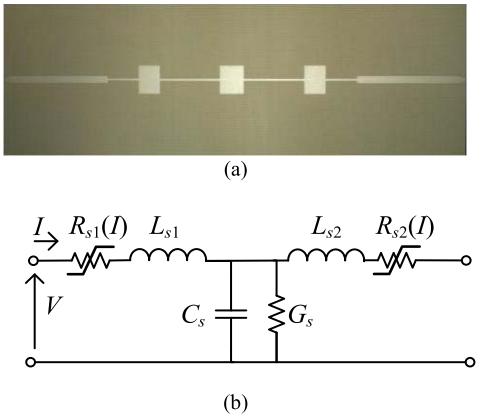

Fig. 11. (a) PCB layout of the LPF, [26]. (b) Equivalent circuit model of a microstrip step discontinuity.

VI. Nonlinear Effects in a Microstrip Filter

Utility of the model of distributed PIM generation in microstrip TL outlined in Section V is illustrated here by application to the analysis of a low-pass stepped-impedance microstrip filter. Fig. 11(a) shows the filter layout comprised of nine sections of uniform microstrip lines of different widths and lengths, and eight step discontinuities. The Butterworth type filter was designed to get maximally flat response and to be well-matched in the E-GSM band (880–960 MHz). The filter and a test coupon of uniform microstrip line were fabricated on a single PCB panel of Laminate A described in Section II. Inspection of the microstrip finish has confirmed high-quality plating with no visually discernible surface contamination. The measured and simulated PIM3 characteristics of the filter are shown in Fig. 12.

Since the filter and the uniform TL coupon were fabricated on the same Laminate A as in Section II by the same PCB workshop and demonstrated similar measured PIM3, we can assume that the microstrip nonlinearity is of resistive type and is satisfactorily described by the modulus polynomial $R(I) = R_0 + R_1|I| + R_2|I|^2$. The parameters of nonlinearity were extracted from the forward PIM3 measurements of the test uniform TL in a range of carrier power levels, as detailed in Section IV, and have the values $R_1 = 2.3 \times 10^{-7}\Omega/(A{\cdot}\mathrm{m})$ and $R_2 = 2.9 \times 10^{-8}\Omega/(\mathrm{A}^2{\cdot}\mathrm{m})$ for each constituent 15° section. They were further scaled with respect to the microstrip width as per (2) in order to calculate the parameters of the equivalent circuit model for each uniform section of the filter. In case when the filter section length was not a multiple of 15°, the nonlinear parameters were rounded to the nearest multiple, which did not incur any noticeable inaccuracy.

The effect of the step discontinuities was associated with a moderate increase of the carrier surface current density at the junctions of the microstrip sections of different widths. Such a current bunching has a minor effect on the distributed PIM generation, thus suggesting that the step discontinuity can be modeled by a conventional nonlinear T-network, [29], consisting of two series nonlinear impedances connected through a shunt linear capacitor shown in Fig. 11(b). The effects of the coupling between the adjacent step discontinuities of wide patches in Fig. 11(a) can, in principle, be incorporated in the equivalent circuit model, [35], thus introducing internal circuit dynamics. However, the discontinuities in our filter layout can be treated as uncoupled, which is justified by the sufficient length of the TL sections and by the absence of the dynamic effects in the frequency-sweep PIM measurements.

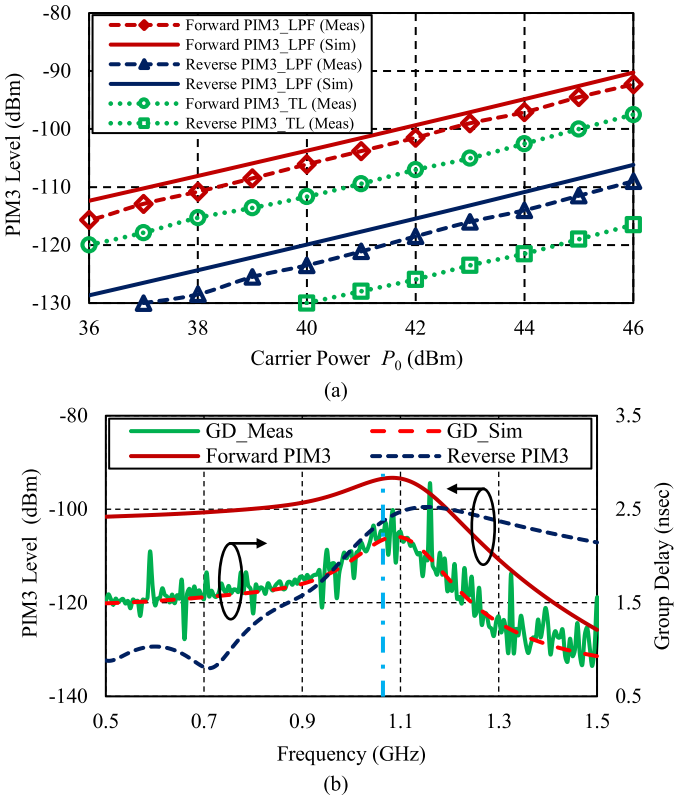

Fig. 12. (a) Measured and simulated PIM3 characteristics of the LPF of Fig. 11(a) and of the reference uniform TL and (b) measured and simulated GD of the simulated forward and reverse PIM3 products. The LPF passband edge is marked by vertical dash-dotted line.

The small-signal equivalent circuit parameters of the step discontinuity in Fig. 11(b) were calculated using the quasi-static approximations, [29]. The nonlinear coefficients of each resistor $R_{s1}(I)$ and $R_{s2}(I)$ in the equivalent circuit model in Fig. 11(b) were deduced from the corresponding TLDN parameters. Alternatively, nonlinear characterization of the microstrip discontinuities could be based on the measured X-parameters, but this approach is not supported by the available commercial PIM analyzers.

The simulated and measured forward and reverse PIM3 products of the filter are shown in Fig. 12(a) versus carrier input power. The results are in good agreement. The magnitudes of the simulated and measured PIM3 products have ∼3 dB offset, which is likely to be caused by fabrication tolerances. Indeed, the preceding PIM measurements on three replicas of microstrip line fabricated on a single panel demonstrated up to 5 dB variation in both forward and reverse PIM3 levels, possibly due to different distributions of the PIM sources. Such an uncertainty affects the extracted model parameters and simulated filter PIM performance.

It was observed previously that PIM response of a filter peaks at the band edges, [17]. Fig. 12(b) shows the simulated and measured group delay (GD) of the low-pass filter (LPF)

against the simulated PIM3 level as the carrier frequencies cross over the passband edge at 1060 MHz. The forward PIM3 peaking correlates with the GD hump crest at the band edge. This effect resembles the nonlinear optical phenomenon of enhanced four-wave mixing in nonlinear periodic media due to phase matching at the bandgap edges, [36]. Interestingly, the reverse PIM peaks at a higher frequency and significantly exceeds the forward PIM in the stopband. Intuitively, this can be explained by the effective penetration depth of the carrier signals into the filter structure in the rejection band. The forward PIM3 products cannot pass, but due to their finite penetration, the reflected carrier signals will generate PIM3 products that add up in phase at the filter input. As the frequency increases, the penetration depth reduces and the reverse PIM3 level decreases. From the design perspective, the long tail of the reverse PIM3 in the filter stopband may cause serious issues in the adjacent frequency bands.

VII. Conclusion

In this paper, we presented a new approach to characterization of distributed nonlinearities in printed TLs fabricated on commercial microwave laminate materials. The developed model was applied to the PIM analysis of the microstrip TL nonlinearity caused by the "black-tin" contamination of the signal track edges.

The closed-form phenomenological model of distributed PIM generation was devised under the assumption of polynomial type of nonlinearities in different parameters of the TLs. The effects of the TL geometry were consistently taken into account as the model parameters were retrieved from the sweep power measurements of forward PIM3 products. It has been demonstrated that high-order polynomial approximations were necessary for adequate prediction of the PIM products in a wide range of carrier power. An alternative model, based on the modulus type polynomials, was proposed and applied to PIM product simulations. It has been demonstrated that the new model requires much lower order polynomials, while providing accurate description of the resistive nonlinearities in the TL.

The presented models of nonlinearities were implemented in the Keysight ADS software that enabled great flexibility in the analysis and characterization of PIM generation in realistic printed circuit devices. In particular, this approach was illustrated by identification and modeling of the effects of nonuniform distribution of PIM sources on microstrip TLs. Moreover, the software-based modeling proved to be indispensable for simulation of the PIM response in complex circuit layouts. Utility of the developed models and their integration with Keysight ADS simulator was proven by the analysis of the PIM performance of a microstrip filter.

From the design point of view, it is important to understand how the PIM generation in the filter can be reduced without compromising an optimum small-signal performance. One may be tempted to examine the current distributions at the carrier frequencies and redesign (e.g., increase the microstrip width) the sections with the highest current density. Although such an approach may yield improvement in some filter topologies, in general the problem of minimizing PIM by layout design requires a holistic approach, due to the distributed nature of the PIM sources. Since optimum filter design under the linearity constraints is beyond the scope of this paper, interested readers are referred to [13], [17], and [18] for further details.

The presented new approach to simulation, analysis and prediction of the PIM performance of passive nonlinear circuit and devices also provides insight in the design optimization under linearity constraints.

Acknowledgment

The authors would like to thank C. Entsfellner and a staff from Rosenberger Hochfrequenztechnik GmbH and Co. KG for their support with the key measurement equipment, and Dr. E. Doumanis from the Nokia Bell Labs, Ireland, for the very fruitful discussions of the filter design and characterization.

References

[1] F. Kearney and S. Chen, "Passive intermodulation (PIM) effects in base stations: Understanding the challenges and solutions," Analog Dialogue, vol. 51, pp. 1–7, Mar. 2017, Accessed: Jun. 5, 2017. [Online]. Available: http://www.analog.com/en/analog-dialogue.html

[2] A. Shayegani, J. Salmon, and R. R. Singh, "Multicarrier PIM behavior and testing in communications satellites," presented at the 32nd AIAA Int. Commun. Satellite Syst. Conf. (ICSSC), San Diego, CA, USA, Aug. 2014.

[3] I. Timmins. (Mar. 2017). "Low passive intermodulation distortion in SATCOM," *Milsat Mag.*, Accessed: Jun. 5, 2017. [Online]. Available: http://www.satmilmagazine.com/story.php?number=1878773008

[4] G. H. Stauss, "Intrinsic sources of IM generation," Naval Res. Lab., Washington, DC, USA, Tech. Rep. 4233, 1980, ch. 5, pp. 65–82.

[5] A. P. Foord and A. D. Rawlins, "A study of passive intermodulation interference in space if hardware," Univ. Kent Canterbury, Canterbury, U.K., ESTEC Contract 111036 Final Rep., May 1992.

[6] R. Hartman, "Measuring the passive intermodulation performance of RF cable assemblies," Kaelus Inc., Hayden, ID, USA, White Paper, 2011, pp. 1–7, Accessed: Jun. 5, 2017. [Online]. Available: http://www.kaelus.com/en/specials-folder/pdf-files/wp_performance_rf_cable_assemblies

[7] J. Miall, "Vector measurements of passive intermodulation products," in *Conf. Precision Electromagn. Meas. Dig.*, London, U.K., Jun./Jul. 2004, pp. 420–421.

[8] J. R. Wilkerson, K. G. Gard, and M. B. Steer, "Automated broadband high-dynamic-range nonlinear distortion measurement system," *IEEE Trans. Microw. Theory Techn.*, vol. 58, no. 5, pp. 1273–1282, May 2010.

[9] D. A. Bradley, "Passive intermodulation (PIM) distance-to-fault analyzer and method to resolve distance-to-fault within a constrained receive band," U.S. Patent 8 903 324 B1, Dec. 2, 2012.

[10] L. Tian, H. Han, W. Cao, X. Bu, and S. Wang, "Adaptive suppression of passive intermodulation in digital satellite transceivers," *Chin. J. Aeronaut.*, vol. 30, no. 3, pp. 1154–1160, Jun. 2017, doi: 10.1016/j.cja.2017.03.010.

[11] M. A. Megahed and S. M. El-Ghazaly, "Nonlinear analysis of microwave superconductor devices using full-wave electromagnetic model," *IEEE Trans. Microw. Theory Techn.*, vol. 43, no. 11, pp. 173–178, Nov. 1995.

[12] O. G. Vendik, I. B. Vendik, and T. B. Samoilova, "Nonlinearity of superconducting transmission line and microstrip resonator," *IEEE Trans. Microw. Theory Techn.*, vol. 45, no. 2, pp. 173–178, Feb. 1997.

[13] T. Dahm and D. Scalapino, "Analysis and optimisation of intermodulation in high-Tc superconducting microwave filter design," *IEEE Trans. Appl. Supercond.*, vol. 8, no. 4, pp. 149–157, Dec. 1998.

[14] D. Seron, C. Collado, J. Mateu, and J. M. O'Callaghan, "Analysis and simulation of distributed nonlinearities in ferroelectrics and superconductors for microwave applications," *IEEE Trans. Microw. Theory Techn.*, vol. 54, no. 3, pp. 1154–1160, Mar. 2006.

[15] A. Kozyrev *et al.*, "Ferroelectric films: Nonlinear properties and applications in microwave devices," in *IEEE MTT-S Int. Microw. Symp. Dig.*, Jun. 1998, pp. 985–988.

[16] F. Gölden, "Liquid crystal based microwave components with fast response times: material, technology, power handling capability," Ph.D. dissertation, Dept. Elect. Eng. Inf. Technol., Techn. Univ. Darmstadt, Darmstadt, Germany, 2010.
[17] M. I. Salkola, "Intermodulation response of superconducting filters," *J. Appl. Phys.*, vol. 98, no. 2, p. 023907, 2005.
[18] J. Mateu, C. Collado, O. Menendez, and J. M. O'Callaghan, "Nonlinear performance characterization in an eight-pole quasi-elliptic bandpass filter," *Supercond. Sci. Technol.*, vol. 17, no. 4, pp. 359–362, 2004.
[19] S. M. H. Javadzadeh, F. Farzaneh, and M. Fardmanesh, "Nonlinear circuit model for discontinuity of step in width in superconducting microstrip structures and its impact on nonlinear effects," *IEEE Trans. Appl. Supercond.*, vol. 23, no. 2, p. 1301208, Apr. 2013.
[20] J. J. Xia, J. A. Kong, and R. T. Shin, "A macroscopic model of nonlinear constitutive relations in superconductors," *IEEE Trans. Microw. Theory Techn.*, vol. 42, no. 10, pp. 1951–1957, Oct. 1994.
[21] J. R. Wilkerson, K. G. Gard, A. G. Schuchinsky, and M. B. Steer, "Electro-thermal theory of intermodulation distortion in lossy microwave components," *IEEE Trans. Microw. Theory Techn.*, vol. 56, no. 12, pp. 2717–2725, Dec. 2008.
[22] J. R. Wilkerson, P. G. Lam, K. G. Gard, and M. B. Steer, "Distributed passive intermodulation distortion on transmission lines," *IEEE Trans. Microw. Theory Tech.*, vol. 59, no. 5, pp. 1190–1205, May 2011.
[23] D. S. Kozlov *et al.*, "Passive intermodulation of analog and digital signals on transmission lines with distributed nonlinearities: Modelling and characterization," *IEEE Trans. Microw. Theory Techn.*, vol. 64, no. 5, pp. 1383–1395, May 2016, doi: 10.1109/TMTT.2016.2550046.
[24] J. Sombrin, P. Michel, G. Soubercaze-Pun, and I. Albert, "Memristors as non-linear behavioral models for passive inter-modulation simulation," in *Proc. 9th Eur. Microw. Integr. Circuit Conf.*, Rome, Italy, Oct. 2014, pp. 385–388.
[25] D. E. Zelenchuk, A. P. Shitvov, A. G. Schuchinsky, and V. F. Fusco, "Passive intermodulation in finite lengths of printed microstrip lines," *IEEE Trans. Microw. Theory Techn.*, vol. 56, no. 11, pp. 2426–2434, Nov. 2008.
[26] A. Shitvov and D. Kozlov, "Nonlinear characterisation for microstrip filters with low passive intermodulation," in *Proc. Integr. Nonlinear Microw. Millimetre-Wave Circuits Workshop (INMMiC)*, Graz, Austria, Apr. 2017, pp. 1–3, doi: 10.1109/INMMIC.2017.7927323.
[27] C. Collado, J. Mateu, and J. M. O'Callaghan, "Analysis and simulation of the effects of distributed nonlinearities in microwave superconducting devices," *IEEE Trans. Appl. Supercond.*, vol. 15, no. 1, pp. 26–38, Mar. 2005.
[28] J. Mateu *et al.*, "Third-order intermodulation distortion and harmonic generation in mismatched weakly nonlinear transmission lines," *IEEE Trans. Microw. Theory Techn.*, vol. 57, no. 1, pp. 10–18, Jan. 2009.
[29] K. C. Gupta, R. Garg, I. Bahl, and P. Bhartia, *Microstrip Lines and Slotlines*, 2nd ed. Norwood, MA, USA: Artech House, 1996.
[30] TINPOSITTM LT-26 Immersion Tin. (2009). *Rohm and Haas Electronic Materials*, Accessed: Jun. 5, 2017. [Online]. Available: http://www.seacole.com/wp-content/uploads/2016/05/Tinposit-LT-26-Immersion-Tin-TDS.pdf
[31] Rosenberger Hochfrequenztechnik GmbH & Co. KG. *Passive Intermodulation Analyzers—PIM Test Solutions for All Applications*. Accessed: Jun. 2017. [Online]. Available: www.rosenberger.com/pia
[32] A. P. Shitvov, D. E. Zelenchuk, A. G. Schuchinsky, and V. F. Fusco, "Passive intermodulation in printed lines: Effects of trace dimensions and substrate," *IET Microw., Antennas Propag.*, vol. 3, no. 2, pp. 260–268, Mar. 2009.
[33] Keysight Technol. *Keysight EEsof EDA Advanced Design System*. Accessed: Jun. 5, 2017. [Online]. Available: http://literature.cdn.keysight.com/ litweb/pdf/5988-3326EN.pdf
[34] D. Kozlov, A. Shitvov, and A. Schuchinsky, "Polynomial model for high-order and multi-carrier passive intermodulation products," in *Proc. 46th Eur. Microw. Conf.*, London, U.K., Oct. 2016, pp. 631–634.
[35] F. Giannini, G. Bartolucci, and M. Ruggieri, "Equivalent circuit models for computer aided design of microstrip rectangular structures," *IEEE Trans. Microw. Theory Techn.*, vol. 40, no. 2, pp. 378–388, Feb. 1992.
[36] C. Becker, M. Wegener, S. Wong, and G. von Freymann, "Phase-matched nondegenerate four-wave mixing in one-dimensional photonic crystals," *Appl. Phys. Lett.*, vol. 89, no. 13, pp. 131122-1–131122-3, 2006.

Alexey P. Shitvov (M'06) received the Diploma Engineering degree in semiconductor devices and microelectronics from Nizhny Novgorod State University, Nizhny Novgorod, Russia, in 1995, and the Ph.D. degree in electronics and electrical engineering from Queen's University Belfast (QUB), Belfast, U.K., in 2009.

From 2009 to 2014, he was a Royal Academy of Engineering Research Fellow with the ECIT Institute, QUB, where he conducts research on phenomenology and mitigation of passive intermodulation in communication components and systems. He is currently a Lecturer of millimeter-wave and submillimeter-wave passive and active components and devices with the School of Electronics, Electrical Engineering and Computer Science, QUB. His current research interests include characterization and modeling of nonlinearities in communication systems, advanced microwave materials, and millimeter-wave communication and sensing system design under hardware constraints.

Dmitry S. Kozlov received the B.Sc. and M.Sc. degrees in radiophysics from Saint Petersburg Electrotechnical University LETI, St. Petersburg, Russia, in 2009 and 2011, respectively, and the Ph.D. degree in electronics and electrical engineering from Queen's University Belfast (QUB), Belfast, U.K., in 2016.

He was a Marie Curie Early Stage Researcher with the Institute of Electronics, Communications and Information Technology, QUB, from 2013 to 2016. He is currently with Nokia Bell Labs, Dublin, Ireland. His current research interests include microwave and antenna theory, including synthesis of antenna arrays, mechanisms of PIM generation in microwave passive and tunable devices, and wireless energy transfer systems.

Alexander G. Schuchinsky (M'97–SM'05–F'14) received the Ph.D. degree in radiophysics from the Leningrad Electrotechnical Institute, St. Petersburg, Russia, the academic title of Senior Research Scientist (USSR).

He was a Leading Scientist with the Microwave Electrodynamics Laboratory, Rostov State University, Rostov, Russia, and a Chief Engineer at Deltec-Telesystems, Wellington, New Zealand. From 2002 to 2015, he was with the School of Electronics, Electrical Engineering and Computer Science, Queen's University of Belfast, Belfast, U.K. He is currently an Honorary Fellow with the Department of Electrical Engineering and Electronics, University of Liverpool, Liverpool, U.K. He has authored 3 international patents, 4 book chapters, and over 200 refereed journal and conference papers. His current research interests include physics-based modeling of linear and nonlinear phenomena in complex electromagnetic structures, metamaterials and nonreciprocal devices; passive intermodulation effects; and characterization of electromagnetic materials.

Dr. Schuchinsky was a corecipient of the IEEE 2010 Microwave Prize and recipient of the 2012 V. G. Sologub Award for contribution to computational electromagnetics. He was a co-founder and a General Co-Chair of the annual conference series "Metamaterials: International Congress on Advanced Electromagnetic Materials in Microwaves and Optics" and is a member of the Board of Directors of the Virtual Institute for Artificial Electromagnetic Materials and Metamaterials, "Metamorphose VI."